ACS APPLIED MATERIALS & INTERFACES

www.acsami.org

Research Article

A Novel and Sustainable Approach to Enhance the Li-Ion Storage Capability of Recycled Graphite Anode from Spent Lithium-Ion Batteries

Madhushri Bhar, Udita Bhattacharjee, Dhritismita Sarma, Satheesh Krishnamurthy, Kaliprasad Yalamanchili, Arup Mahata,* and Surendra K. Martha*

Cite This: *ACS Appl. Mater. Interfaces* 2023, 15, 26606−26618

Read Online

ACCESS | Metrics & More | Article Recommendations | Supporting Information

ABSTRACT: The ubiquitous manufacturing of lithium-ion batteries (LIBs) due to high consumer demand produces inevitable e-waste that imposes severe environmental and resource sustainability challenges. In this work, the charge storage capability and Li-ion kinetics of the recovered water-leached graphite (WG) anode from spent LIBs are enhanced by using an optimized amount of recycled graphene nanoflakes (GNFs) as an additive. The WG@GNF anode exhibits an initial discharge capacity of 400 mAh g^{-1} at 0.5C with 88.5% capacity retention over 300 cycles. Besides, it delivers an average discharge capacity of 320 mAh g^{-1} at 500 mA g^{-1} over 1000 cycles, which is 1.5−2 times higher than that of WG. The sharp increase in electrochemical performance is due to the synergistic effects of Li-ion intercalation into the graphite layers and Li-ion adsorption into the surface functionalities of GNF. Density functional theory calculations reveal the role of functionalization behind the superior voltage profile of WG@GNF. Besides, the unique morphology of spherical graphite particles trapping into graphene nanoflakes provides mechanical stability over long-term cycling. This work explains an efficient strategy to upgrade the electrochemical compatibility of recovered graphite anode from spent LIBs toward next-generation high-energy-density LIBs.

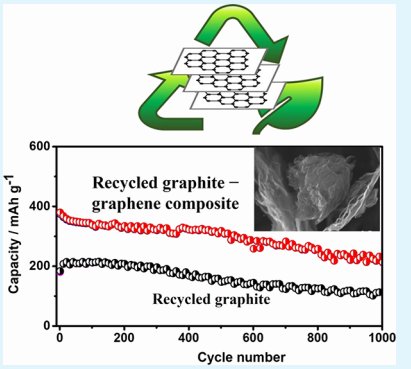

KEYWORDS: *recycling, spent lithium-ion batteries, anode, graphite, graphene nanoflakes, electrochemistry, DFT calculation*

INTRODUCTION

The forefront of battery research in modern civilization aims toward high-power and high-energy-density applications in scientific and industrial fields with reduced cost, improved safety and cycle-life, and superior rate capability. Over the past few decades, lithium-ion batteries (LIBs) have become a leading technology in the emerging sectors of portable electronic and electric vehicle (EV) appliances.[1,2] However, the vast manufacturing of LIBs and the generation of inevitable e-waste after their lifespan have raised significant concerns in economic and environmental prospects.[3] The global LIB market value is anticipated to reach $139 billion by 2029 to fulfill the ever-growing consumer demand.[4] It may produce over 11 million tons of discarded LIBs between 2017 and 2030.[5] This emphasizes the need for developing novel recycling strategies for the spent LIB components.

Graphite is a state-of-art commercialized anode material due to its low lithiation potential (<100 mV), high conductivity, and high electrochemical stability (>1000 cycles). The governments of the United States of America and Europe have classified graphite as a critical mineral for increasing the demand by 10−12% every year.[6] To date, the price of graphite has become $20/kg.[7] The market value of graphite is forecast to hit $21.6 billion by 2027 with a CAGR of 5.3%.[8] Current LIB recycling strategies mainly focus on cathode recovery for valuable metals (Li, Co, etc.).[9,10] In the pyrometallurgy process, the carbon anode is burnt in a smelter furnace to recover the cathode by carbothermal reduction. During this process, the carbon anode is oxidized into CO_2 (a poisonous gas) and Li_2CO_3 (as slag); thus, graphite cannot be recovered.[11] Meanwhile, in hydrometallurgy, carbon is settled down during solvent extraction and separation. The recovered carbon by this method is of poor quality and needs high production costs for battery-grade applications.[4,12] In comparison, the physical dismantling process is effective for graphite recovery, although this process is challenging for scaling up to the industry level.

However, the theoretical capacity of graphite is limited to 372 mAh g^{-1} (corresponding to the LiC_6 phase), and it fails to

Received: February 16, 2023
Accepted: May 11, 2023
Published: May 25, 2023

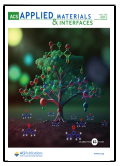

Scheme 1. Flowchart of the Overall Regenerating Process of Graphite Anode

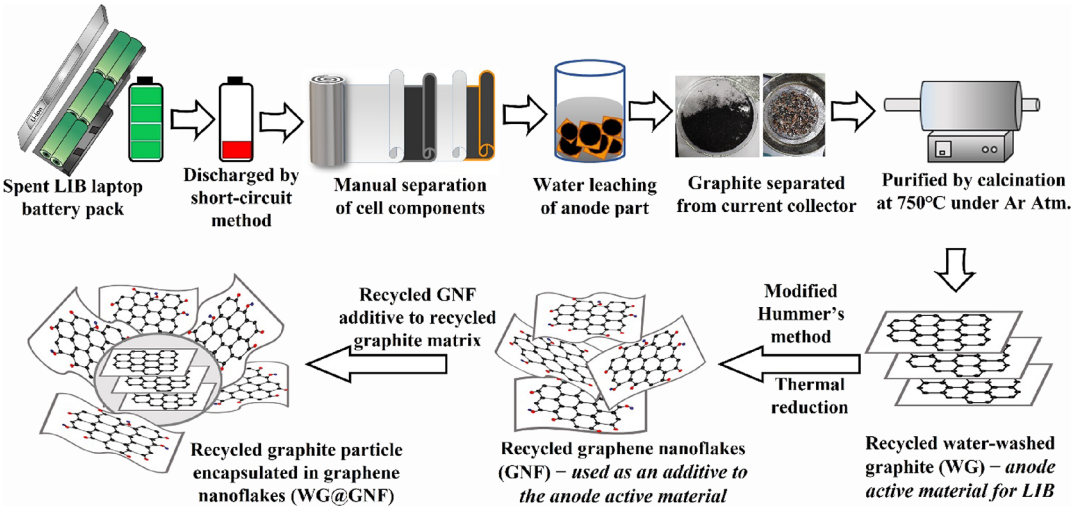

compete with the ongoing energy crisis. Besides insertion-type anodes, alloys, and conversion-type materials (theoretical capacity of ~1000 mAh g^{-1}),[13,14] various advanced carbonaceous materials like graphene, carbon nanotube (CNT), carbon nanofiber (CNF), hard carbon, etc., have been studied extensively to reveal Li-ion storage properties. Among them, 2D nanostructured graphene stole the limelight as LIB anode because of the incredible electronic transport phenomenon, flexibility, conductivity, wide electrochemical window, and more Li-ion storage capability.[15] This results in a high capacity of 744, 780, and 1114 mAh g^{-1} for the formation of LiC_3, Li_2C_6, and LiC_2, respectively, depending on Li^+ intercalation and adsorption in both sides and edges of graphene sheets.[16,17] However, the literature reports the limited cyclability of graphene anode alone within hundreds of cycles with ~50% capacity loss due to irreversible Li^+ trapping and aggregation of graphene sheets, although it delivers high capacity during the initial cycle. Besides, the large-scale synthesis of graphene due to the very low-density material and high irreversible capacity loss (>50%) restricts the commercialization of graphene batteries. Meanwhile, compositing graphene with carbonaceous materials (e.g., carbon nanofiber, CNT, and graphite foil) can enhance electrochemical performance as illustrated in Supporting Information Table S1 in terms of charge−discharge cycling stability and capacity retention with respect to the cycle number in comparison to our study with recycled graphite material.[18−22]

Generally, the degradation of graphite anode on prolonged cycling is attributed to the formation of a thick solid electrolyte interface (SEI) layer on the graphite surface due to the reductive decomposition of electrolyte solvents and salt anions.[23,24] The SEI layer and solvated Li-ion create pressure that results in the cracking and splitting of graphite flakes. The damaged, exposed surfaces are prone to further surface reactions, which deteriorate the cell performance. In a cycled graphite, the layers can expand up to 10.3%.[18] The bulk structural integrity and crystal lattice of the graphitic matrix are still retained. Therefore, after some postpurifications, the recovered graphite can be reused as an anode material for LIBs. In the reported literature, the black mass recovery and electrochemical activity of electrode materials are restored by acid leaching (H_2SO_4-H_2O_2, HCl-H_2O_2, organic acids, etc.), NMP, or microwave-assisted deep eutectic solvent based leaching.[4,25−34] Herein, we focus on improvising the electrochemical performance of water-leached recovered graphite by using a conductive additive to the recovered graphite matrix instead of any acidic solvent washing, as reported earlier.

A recent publication from our group observed that graphite is recovered from spent laptop battery packs by a facile water leaching method[35] and further calcined under an inert atmosphere at 750 °C to eliminate residual impurities and improve the degree of graphitization of the recovered graphite. Recovered water-washed graphite (WG) delivered a stable discharge capacity of 310 mAh g^{-1} at 0.1C rate over 100 cycles and 295 mAh g^{-1} at 0.5C rate over 1000 cycles, respectively.[36] Herein, the specific capacity of WG is further improvised by compositing with graphene nanoflakes (GNFs) as a conductive additive synthesized from WG by the modified Hummer's method. Electrochemistry reveals that optimized WG@GNF displays superior C-rate performance and an average discharge capacity of 320 mAh g^{-1} with 62% capacity retention over 1000 cycles (156 mAh g^{-1} for WG) at a higher current density of 500 mA g^{-1}. Experimental characterizations coupled with DFT calculations reveal that the higher reversible Li-ion storage with the voltage profile is attributed to the synergistic phenomena of Li-ion intercalation and adsorption into the tailored surface functionalized WG@GNF. To check the potential feasibility of WG@GNF as the anode, full cells are fabricated with commercial NMC 811 and LFP cathodes. This study reveals the comprehensive utilization of graphite anode from spent LIBs and improvements in its specific capacity through precise compositing with graphene nanoflakes, which pave the way for a promising active anode material for high-performance Li-ion batteries.

EXPERIMENTAL METHODS

Graphite Recovery from Spent LIBs and Postpurification. Spent lithium-ion laptop batteries were provided by Nile Limited, Hyderabad, India. The 18650-type cylindrical cells were discharged first by the short-circuit method below 2 V for safety issues. The cells were then manually dismantled, and the anode part was carefully segregated from the Swiss roll assembly of the electrode separator. The anode black mass was recovered from the copper foil current collector by water leaching. The binder dissolved, separating the anode black mass from the copper foil current collector. This process eliminates surface-adsorbed lithium and lithium-containing SEI components (e.g., Li_2O, Li-alkyl carbonates, bicarbonates, and

https://doi.org/10.1021/acsami.3c02272
ACS Appl. Mater. Interfaces 2023, 15, 26606−26618

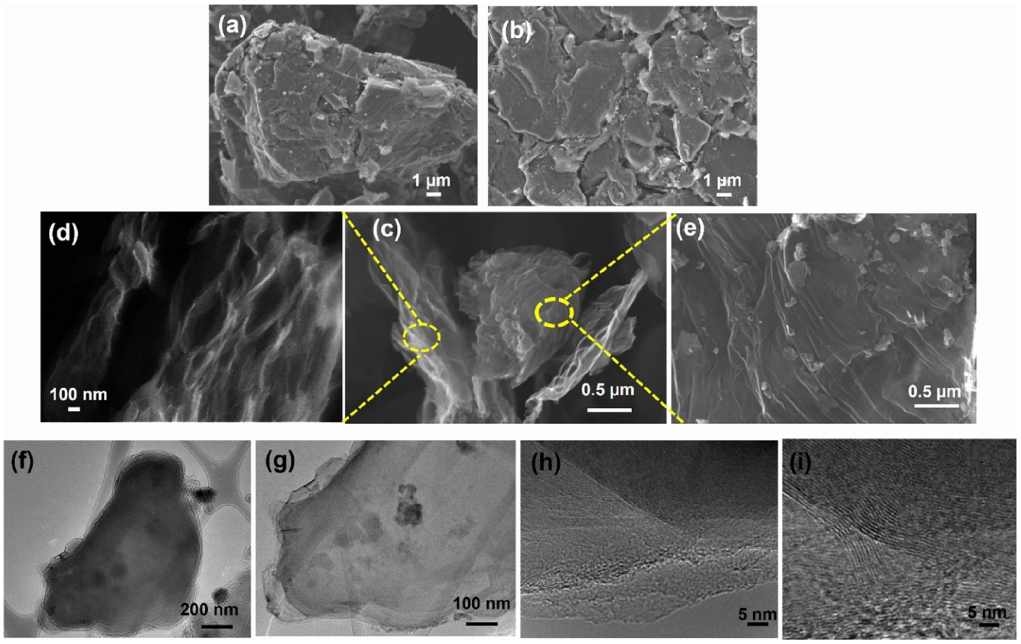

Figure 1. Scanning electron microscopy images of (a) recovered water-washed graphite, (b) water-washed graphite purified by heating under inert condition (WG), and (c) WG@GNF; zoomed image of (d) GNF portion and (e) WG portion; and transmission electron microscopy images of (f–i) WG@GNF.

Li_2CO_3) from the graphite surface by the H_2 evolution reaction.[37] The anode black mass was filtered and dried at 90 °C overnight. It was then calcined at 750 °C for 5 h under an argon atmosphere to eliminate carbon black additives, Li-salts, and electrolyte-decomposed impurities from the graphite surface. This purified graphite is termed water-washed graphite (WG).

Synthesis of Graphene Nanoflakes (GNFs) from Recycled Graphite. GNF was synthesized from WG by the modified Hummer's method.[38] First, 1 g of WG was added to 1 g $NaNO_3$ in 46 mL concentrated H_2SO_4 medium and stirred in an ice bath for 4 h. Next, 6 g of $KMnO_4$ was added and stirred at 35 °C for 2 h. After that, 92 mL of ice-cold DI-water was added and refluxed at 98 °C for 2 h. Finally, 50% H_2O_2 was added and repeatedly washed with 1:3 HCl/water mixture and DI water until a neutral pH was obtained. The resultant graphene oxide (GO) was dried overnight at 70 °C. It was then calcined at 500 °C for 30 min under an inert atmosphere and reduced thermally to graphene nanoflakes (GNFs).

Regeneration of Recovered Water-Washed Graphite. An optimized weight ratio of 20 wt % of recycled GNF was mixed with recovered water-washed graphite (WG) in DI-water solvent, ultrasonicated for 15 min at room temperature, and dried overnight at 70 °C. Here, GNF is used as an additive to the graphite matrix, and the regenerated material is termed WG@GNF. Scheme 1 describes the flowchart of the overall regenerating process of anode graphite.

Structural and Morphological Characterizations. The powder XRD was analyzed by an X'Pert Pro diffractometer (The Netherlands) using Cu Kα radiation (λ = 1.54 Å), reflection θ–θ geometry, a receiving slit of 0.2 mm, a scintillation counter, 30 mA, and 40 kV. The diffraction data were collected between the 2θ angle of 5 and 80°. Raman spectroscopy was conducted using a micro-Raman spectrometer (HR800, Jobin Yovn Horiba, France) with a He-Ne laser of excitation line 632.8 nm and a microscope objective (50×, Olympus MPlan, 0.4 mm working, numerical aperture 0.75 in backscattering configuration). The surface morphologies were carried out by scanning electron microscopy (JEOL-FESEM). FTIR spectroscopy was carried out in a Bruker Alpha-P FTIR spectrometer. XPS was measured using ESCA+ (Omicron Nanotechnology, Oxford Instruments Plc., Germany) equipped with monochromic Al Kα (1486.6 eV) X-ray beam radiation operated at 15 kV and 20 mA. The binding energy was calibrated *vs* carbon (C 1s = 284.6 eV).

Cell Assembly and Electrochemical Characterizations. The electrochemical performances were determined in CR2032-type coin cells. The slurry composition was 90 wt % of the graphite-based anode active material and 10 wt % PVDF binder (Kureha 1700) in NMP solvent. The slurry was coated onto a copper foil current collector using a doctor blade. Electrodes were dried overnight at 80 °C under a vacuum and calendared followed by punching into a circular disc of 10 mm diameter. The active material loading was 1.2 ± 0.3 mg cm^{-2}. The coin cells were fabricated inside a glove box (mBraun, Germany) with O_2 and H_2O levels less than 0.1 ppm. The pure-Li metal chip was used as a reference and counter electrode half-cell study, and the electrolyte is 1 M $LiPF_6$ in ethylene carbonate-diethyl carbonate solvent. The electrochemical analysis, such as charge–discharge cycling and C-rate performance at different current densities for the electrode, was carried out using Arbin battery testing instruments (Arbin BT2000-Battery test equipment). Cyclic voltammetry and impedance studies were performed in the cell test system model 1470E coupled with an FRA model 1455A (Solartron Analytical Oak Ridge, TN) instrument.

Computational Details. First-principles calculations based on density functional theory (DFT) were carried out as implemented in the PWSCF Quantum-Espresso package.[39] Geometry optimization, including dispersion correction,[40] was performed using the GGA-PBE[41] level of theory, and the electron–ion interactions were described by ultrasoft pseudo-potentials with electrons from C 2s, 2p; O 2s, 2p; Li 2s; shells explicitly included in calculations. Plane-wave basis set cutoffs for the smooth part of the wave functions and the augmented density were 25 and 200 Ry, respectively. Both ions and volume were relaxed during the optimization of the bulk structures. Geometry optimizations for the 6 × 6 × 2 supercell were performed with a *k*-point[42] sampling of 3 × 3 × 3 for both graphite and composite models. Composite models were constructed by functionalizing one layer of bulk 6 × 6 × 2 supercell graphite with oxygen atoms (explained in detail in Supporting Information Text S1 and Figure S1).

The binding energy of the Li atom was calculated using the following relation:

$$E_{\text{Binding}} = E_{C_{288}Li_x} - E_{C_{288}} - xE_{\text{Li}}$$

https://doi.org/10.1021/acsami.3c02272
ACS Appl. Mater. Interfaces 2023, 15, 26606–26618

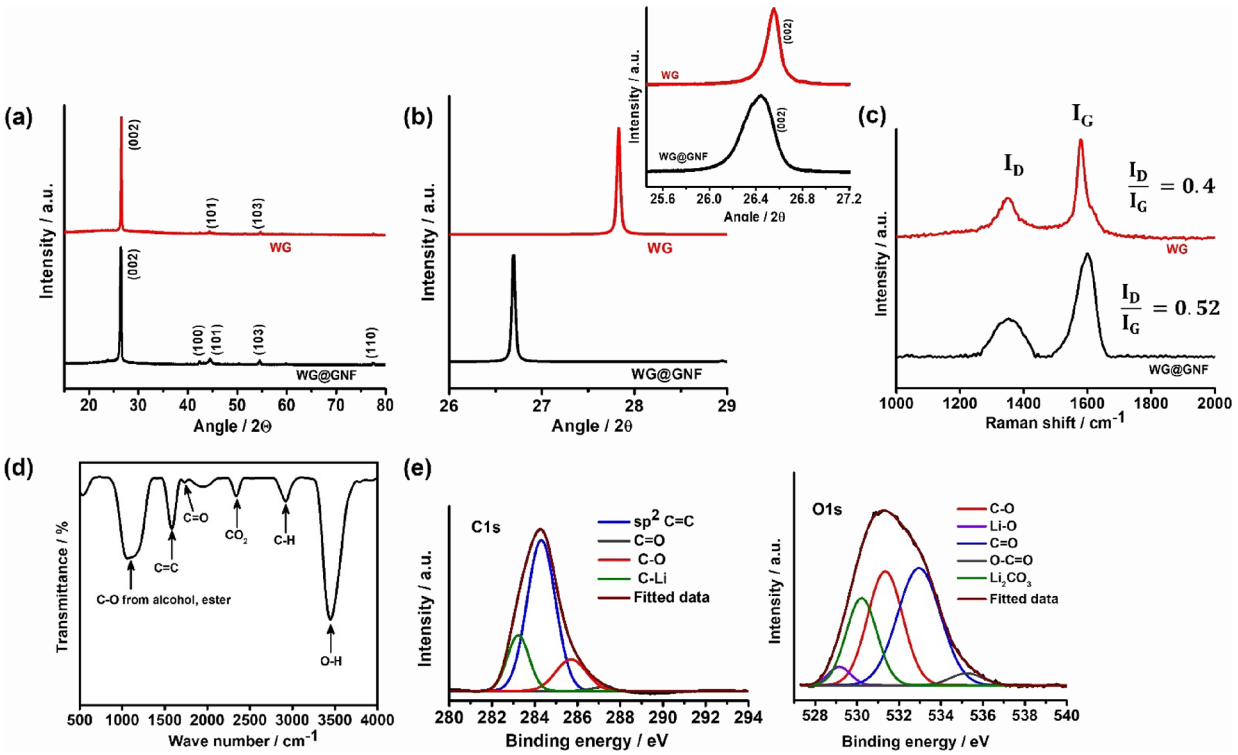

Figure 2. (a) X-ray diffraction patterns, (b) simulated XRD (inset: peak position of (002) plane in the experimental), (c) Raman spectra of WG@GNF and WG, (d) FTIR spectra, and (e) XPS plots of WG@GNF for C 1s and O 1s.

where $E_{C_{288}Li_x}$ is the energy of the bulk Li atom intercalated graphite, xE_{Li} is the energy of the Li atoms, and $E_{C_{288}}$ is the energy of the bulk graphite. The average voltage (V) during the Li intercalation process (xLi + C_{288} → Li_xC_{288}, where x is the number of Li intercalated into graphite) can be written in the form of the change in Gibbs free energy (ΔG_f):[43−46]

$$V = -\frac{\Delta G_f}{zF}$$

where z and F are the number of valence electrons during the intercalation process and the Faraday constant, respectively, and ΔG_f is the change in Gibbs free energy during the intercalation process, which is defined as

$$\Delta G_f = \Delta E + P\Delta V - T\Delta S$$

$P\Delta V$ is on the order of 10^{-5} eV, and the term $T\Delta S$ is comparable to 26 meV at room temperature; thus, the entropy and pressure terms are negligible.[43,44,46] ΔG_f is then approximately equal to the total energy change (ΔE) involved in the system, which is defined as

$$\Delta E = E_{Li_xC_{288}} - E_{Li_x} - E_{C_{288}}$$

where $E_{Li_xC_{288}}$ is the total energy of the Li intercalated graphite system, E_{Li_x} is the energy of intercalated Li-atoms, and $E_{C_{288}}$ is the energy of the pristine graphite system, respectively. Therefore, the voltage is given by the equation

$$V = -\frac{E_{Li_xC_{288}} - E_{Li_x} - E_{C_{288}}}{zx}$$

Similarly, for the composite system, the voltage was calculated by the following equation:

$$V = -\frac{E_{Li_xC_{288}O_{12}} - E_{Li_x} - E_{C_{288}O_{12}}}{zx}$$

Specific capacity was calculated using the following equation:[47,48]

$$C = \frac{nxF}{M_f}$$

where n is the number of electrons transferred per formula unit, x is the number of Li atoms intercalated, F is the Faraday constant, and M_f is the mass of the formula unit. Charge difference distribution (CDD) was obtained using the following equation:[49,50]

$$\rho_{CDD} = \rho_{Total} - \sum_i \rho_i^{Fragments}$$

where ρ_{Total} is the total charge density of the system and $\rho_i^{Fragments}$ represents the charge density of the individual fragments.

RESULTS AND DISCUSSIONS

Morphological and Structural Characterizations. SEM analysis is conducted to understand the morphological characteristics of pristine recovered and reformed graphite. Figure 1a shows the water-washed recovered graphite with the agglomeration of graphite particles having secondary impurities on the surface of the graphite particles. However, the roughness of the graphite surface is diminished, and the electrolyte decomposed products are eliminated on thermal treatment, as shown in Figure 1b. Further, to understand the effect of washing upon impurity removal, we have conducted the elemental mapping analysis of scrapped graphite (without washing) and the purified graphite. The elemental mapping of scraped graphite (Supporting Information Figure S2a) shows the presence of O, F, and P elements in addition to C due to the SCMC binder, $LiPF_6$ salt, and electrolyte decomposed products. After purification, O, F, and P elements reduce in WG, showing the strong presence of C (Supporting Information Figure S2b). Besides, spherical graphite particles are trapped in the wrinkled graphene flakes,[19] as shown in the surface microstructure of WG@GNF in Figure 1c. Figure 1d is the magnified image of Figure 1c that shows the flocculent

https://doi.org/10.1021/acsami.3c02272
ACS Appl. Mater. Interfaces 2023, 15, 26606−26618

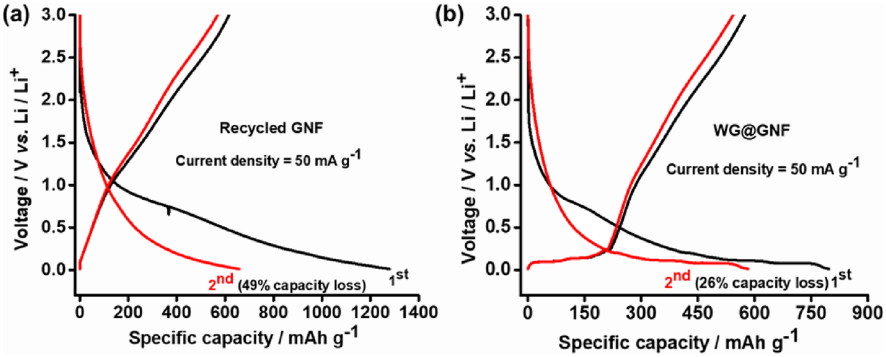

Figure 3. Galvanostatic charge−discharge voltage profile of (a) recycled GNF and (b) WG@GNF at a lower current density of 50 mA g^{-1}.

morphology of wrinkled graphene nanoflakes. Similarly, Figure 1e is the magnified image of Figure 1c, where the smooth surface and graphite flakes are visible. EDS mapping of WG@GNF (Supporting Information Figure S2c) further confirms the uniform distribution of elemental O in the carbon matrix, and the atomic % of carbon and oxygen is 84.4 and 15.6%, respectively. Besides, TEM images also validate similar morphologies. Figure 1f,g shows the overall particle and edge view of WG@GNF, indicating that the spherical graphite particle is encapsulated within thin graphene layers. Figure 1h,i is the magnified boundary image with clear visibility of the ordered layered arrangement of graphite layers and randomly oriented graphene sheets of WG@GNF. This unique morphology might facilitate the infiltration of the electrode material and reduce the agglomeration of graphene flakes that might provide structural integrity during the electrochemical charge−discharge cycling process. Supporting Information Figure S3a,b presents the TEM images of as-synthesized recycled graphite (WG) and recycled graphene nanoflakes (GNFs), respectively.

The XRD pattern of WG@GNF in Figure 2a is compared with the pristine recycled graphite WG. The appearance of a sharp peak at $2\theta = 26.5°$ for the (002) plane (JCPDS #00-056-0159) confirms that the hexagonal crystal system is retained in the recovered graphite. However, the peak broadens in WG@GNF and shifts to a lower 2θ angle for disordered graphene sheets. The interplanar spacing (d_{002}) is increased from 3.35 Å for WG to 3.37 Å for WG@GNF. The peaks at 42.3° for the (100) plane and 44.5° for the (101) plane arise as a result of the hexagonal phase of exfoliated graphite sheets in WG@GNF, which are insignificant in WG (Figure 2b). However, these peaks are more widened in bare recycled GNF, as shown in Supporting Information Figure S4, with an enlarged interplanar spacing d_{002} of 3.65 Å. d_{002} is calculated based on Bragg's equation ($2d \sin\theta = n\lambda$).

We have simulated the X-ray diffraction pattern of the DFT-optimized WG and WG@GNF systems (Supporting Information Figure S5). As seen from Figure 2b, the 2θ value is less in WG@GNF, which matches the trend of the experiment. However, the relative change of 2θ between WG and WG@GNF is more in theory (differs by 2θ of 1.1) than in the experiment (varies by 2θ of 0.2). The difference might be due to the consideration of a single functionalized graphite layer in the simulation model, whereas in the experiment, the functionalized layers are composed of nanoflake morphology; thus, a more packed nature of the functionalized layers is expected. Nevertheless, the lesser 2θ value in composite structures represents the increase in lattice volume compared to graphite structures. This is similar to the experimental trend in which an increased lattice volume was observed as a result of functionalization.

Raman spectroscopy (Figure 2c) is carried out for WG@GNF and WG to understand the distinct structural features and vibrational modes in terms of defects and disorders in the graphitic lattice. The spectra display two strong peaks at 1580 and 1350 cm^{-1} originating from the G-band (attributed to in-plane stretching vibrations of sp^2 carbons) and D-band (corresponding to disordered carbon at the edges and defect sites), respectively. The D-band (I_D) and G-band (I_G) ratios slightly increased from 0.4 for WG to 0.52 for WG@GNF. It indicates the presence of disorderness arising from GNF as a result of the exfoliation of graphene layers, defect sites, and surface functionalities.

The nature of the functional groups present in WG@GNF is investigated by the Fourier transform infrared (FTIR) spectrum (Figure 2d) analysis indicating the bonding nature and composition of the carbon matrix. The characteristic peak at 1630 cm^{-1} denotes in-plane vibration of C═C stretching from sp^2 hybridized graphitic carbons. The peak at 1735 cm^{-1} might be from C═O groups of −COOH. The broad peak at ∼1000 cm^{-1} is related to C−O containing different functional groups originating from oxidized carbon at edges like alcohols, carboxyl, esters, etc. The peak at 3400 cm^{-1} arises from H-bonded −OH stretching.

X-ray photoelectron spectroscopy is conducted to validate further these functional groups' bonding, composition, and surface chemistry in WG@GNF, as shown in Figure 2e. The notable peaks in C 1s spectra at 283.2, 284.8, 285.7, and 287.2 eV correspond to C−Li linkage (from Li intercalation compounds LiC_6), C−C (sp^2 carbon), C−O (epoxide and hydroxyl groups), and C═O (alkyl carbonates), respectively. Besides, in O 1s spectra, the peaks at ∼531.4, 532.9, and 535 eV denote C−O, C═O, and O−C═O linkages. In addition, peaks at 529.1 and 530 eV arise as a result of Li_2O and Li_2CO_3 inorganics from SEI components in cycled graphite. The surface chemistry affirms the presence of controlled oxygen functionalities in the graphite matrix that might directly influence the electrochemical performance of the regenerated graphite material from spent LIBs. Thus, it projects WG@GNF as a promising anode for high-performance LIBs.

Electrochemical Characterizations. In a recent study, we observed that water-washed recycled graphite (WG) exhibits an average discharge capacity of 315 mAh g^{-1} at 0.1C. The capacity of graphite originates from Li-ion intercalation into the layers and the formation of stable lithium intercalation compound LiC_6, corresponding to the maximum theoretical

https://doi.org/10.1021/acsami.3c02272
ACS Appl. Mater. Interfaces 2023, 15, 26606−26618

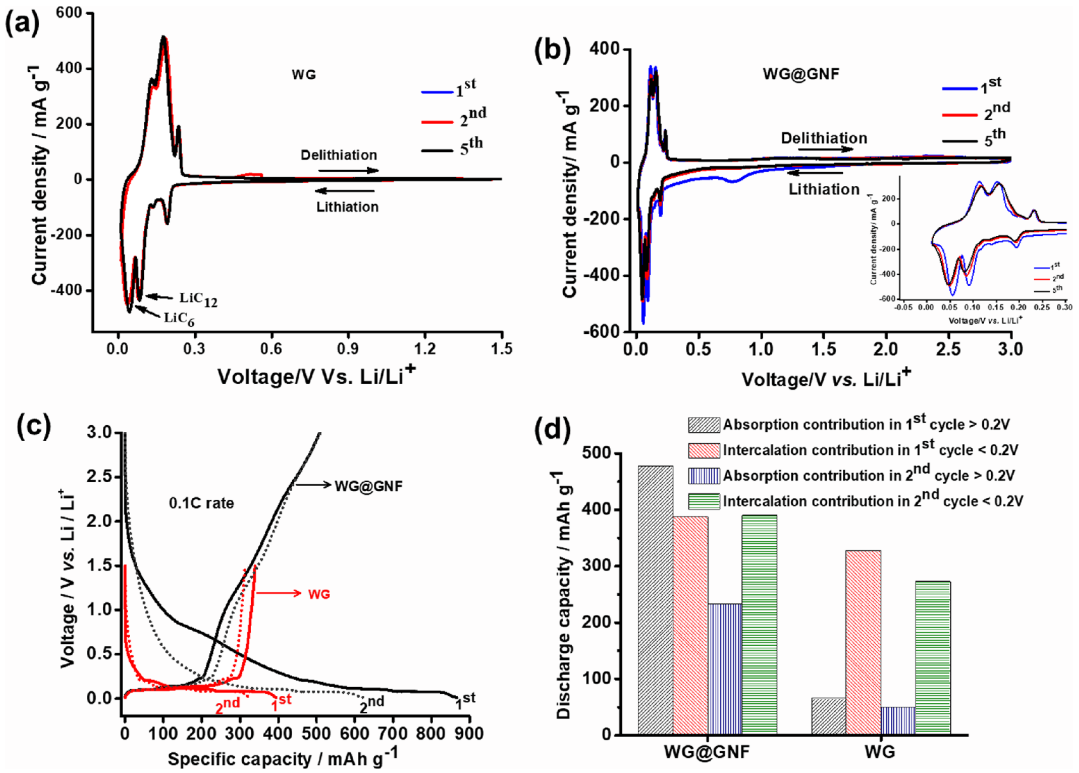

Figure 4. Cyclic voltammetry plots of (a) WG and (b) WG@GNF, (c) galvanostatic charge−discharge voltage profile of WG@GNF and WG at 0.1C rate, and (d) the histogram quantifying the capacity contribution from surface adsorption >0.2 V and intercalation <0.2 V from panel c.

capacity of 372 mAh g^{-1}. The site-controlled Li^+ diffusivity of WG can be surmounted in graphene-based systems by introducing the optimum amount of oxygen- and hydrogen-containing heteroatom functionalities. To understand the Li-storage behavior of pristine recycled graphene nanoflake (GNF) anode material in LIBs, galvanostatic charge−discharge analysis is carried out at a lower current density of 50 mA g^{-1}. Figure 3a shows that recycled GNF delivers an initial discharge capacity of 1280 mAh g^{-1} with 48% Coulombic efficiency (CE). However, in the second cycle, capacity fades deeply to 50% with 658 mAh g^{-1}. The very high initial capacity is attributed to the surface adsorption of Li^+ into pores and defect sites. The irreversibility arises as a result of the solid electrolyte interface (SEI) formation and trapping of Li^+. Such high irreversible capacity during initial cycles is undesirable for practical applications of pure graphene anodes.[15,51] However, the superior Li-storage capability of GNF can be utilized by using an optimized amount of GNF as an additive to recycled water-washed graphite (WG@GNF), minimizing the initial irreversibility. In other words, the capacity of WG will be further enhanced with more numbers of Li-ion accommodation sites by intercalation and adsorption phenomena simultaneously. Supporting Information Figure S6a−d shows the capacity *vs* voltage profile of different compositions of the GNF additive (such as 100, 80, 40, and 20%) to the recycled graphite matrix. Further, Supporting Information Table S2 signifies the irreversible capacity loss during discharge and charge in the first cycle and irreversible discharge capacity in the second cycle. The Coulombic efficiency in the first cycle is observed to be improved from 48% (for GNF) to 72% (for 20% GNF additive). Figure 3b shows that the optimized WG@GNF electrode delivers an initial discharge capacity of 800 mAh g^{-1}, and the irreversible capacity reduces to 26% in the second cycle (49% for recycled GNF) under similar conditions. Thus, it is evident that despite the high irreversibility in graphene systems, its charge storage property can be used to enhance the capacity of recycled graphite anode for high-energy-density LIB applications.

The lithiation (discharge) and delithiation (charge) behavior for WG@GNF and WG is evaluated by a cyclic voltammetry study within the voltage window of 0.01−1.5 for WG and 0.01−3 V for WG@GNF and GNF. Figures 4a,b shows the CV plots for WG and WG@GNF, respectively, at a scan rate of 0.05 mV s^{-1}. The notable lithiation peaks below 100 mV indicate the formation of stable Li intercalation phases of LiC_{12} and LiC_6 in both the anodes. An additional hump in WG@GNF at 0.67 V during the first lithiation process arises as a result of the passivating SEI film by reductive decomposition of the electrolyte. The absence of this peak during subsequent cycles indicates the formation of a stable SEI layer that enhances Li^+ passivation to the graphitic surface. Besides, the expanded area of the CV curve around 3 V is attributed to the surface-induced Li^+ adsorption process into edges and defect sites of the graphene flakes (Figure 4b). It results in simultaneous happenings of surface adsorption of GNF and Li^+ intercalation into the graphite layers, which induce extra charge storage capability in WG@GNF. The larger area under the CV curve and higher peak current density signify better Li-ion kinetics in WG@GNF. The CV curve for bare recycled GNF (Supporting Information Figure S7) shows a broad curve during lithiation and delithiation. No distinct peaks for Li intercalation compound formation in recycled GNF indicate surface adsorption property, intercalation as LiC_x, and nanopore filling. The observed charge storage property from CV plots is in good agreement with the galvanostatic charge−discharge voltage profile at the 0.1C rate. Figure 4c exemplifies

https://doi.org/10.1021/acsami.3c02272
ACS Appl. Mater. Interfaces 2023, 15, 26606−26618

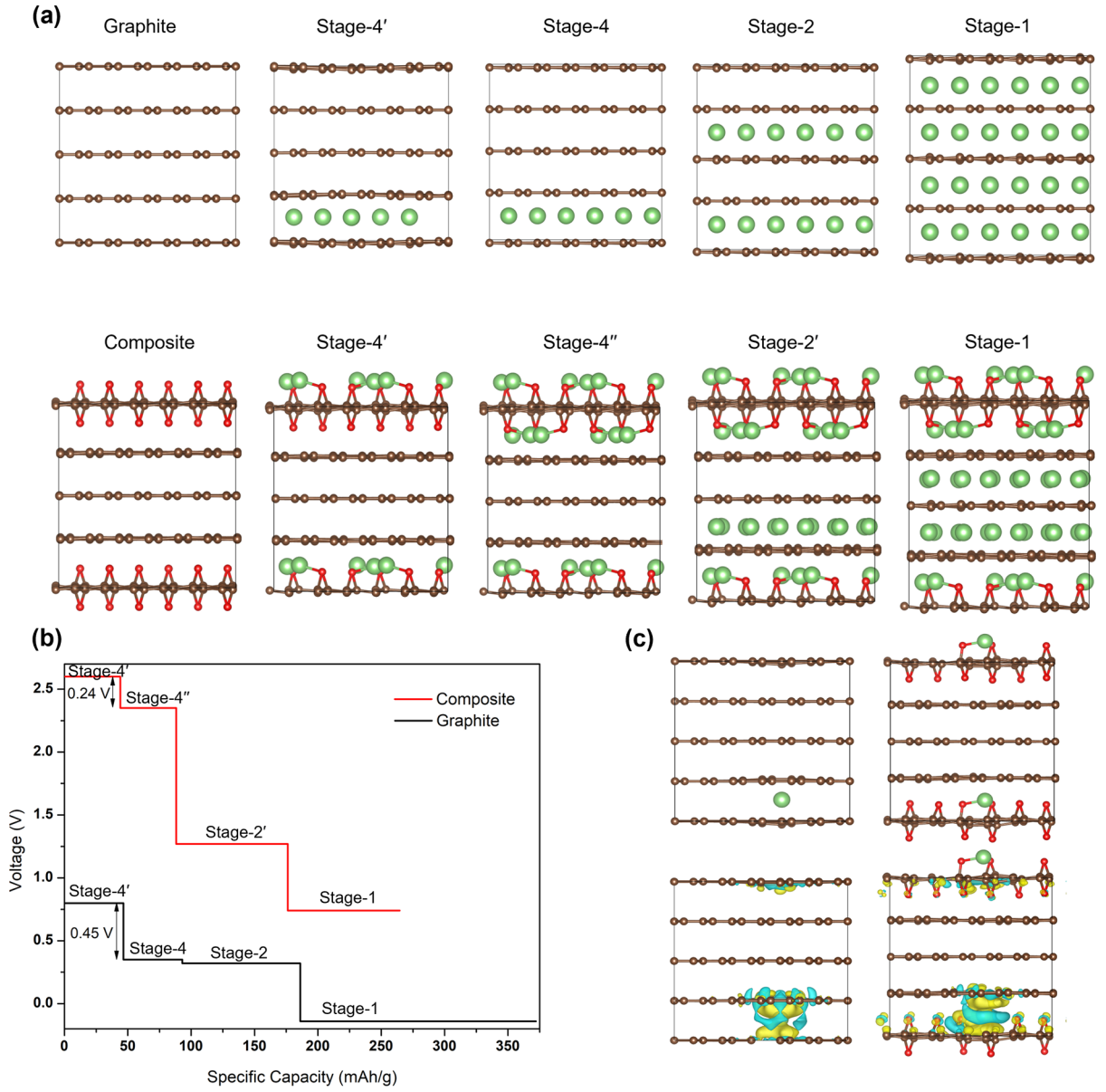

Figure 5. (a) Optimized geometries of WG and WG@GNF composite systems along with the different stages. (b) Voltage profile diagram for the different stages of Li intercalation. (c) Optimized structure with one Li intercalation in graphite and composite structures (upper panel) and the corresponding CDD plot (bottom panel).

the cumulative profiles for WG@GNF and WG at the 0.1C rate, where the unique characteristics of charge storage behaviors can be clearly noticeable. WG@GNF shows an adsorption−intercalation property (866 mAh g^{-1} discharge capacity in the first cycle). In comparison, WG exhibits only a Li intercalation phenomenon (394 mAh g^{-1} discharge capacity in the first cycle) below 0.2 V. Figure 4d presents a histogram that quantifies the capacity contribution from the sloping region (surface adsorption phenomenon >0.2 V) and plateau region (intercalation phenomenon <0.2 V) voltage profiles of WG@GNF in comparison to WG at 0.1C. It signifies that the extra capacity originates from the sloping region surface adsorption of Li^+ into edges and defect sites of graphite sheets in WG@GNF, where the intercalation capacity contribution remains almost the same.

To better understand the voltage profiles, DFT calculation has been performed for the staging mechanism of Li-ion intercalation into the WG and WG@GNF system. This mechanism proceeds through different stages with a varying periodic repeat distances between two neighboring Li-ion intercalant layers. A higher stage number (n) corresponds to a lower intercalant concentration and more empty graphene−graphene layers, implying a lower charge storage capacity.[44,45,52,53] To simulate the staging mechanism, three different stages (stage 4, stage 2, and stage 1) of intercalation are modeled as shown in Figure 5a, considering two different concentrations for stage 4 in both graphite and composite systems. Stage 4 has also been modeled with a lower Li-concentration, which is referred to as stage 4′ in the case of the graphite system. On the other hand, another model is stage 4″, which represents a quasi-stage 4′ Li intercalation, where the Li atoms are intercalated on both sides of the oxygen-functionalized layer. Therefore, considering the $C_6[Li]_x$ formula unit, the x values result in 0.125, 0.25, 0.5 and 1.0 for stage 4′, stage

https://doi.org/10.1021/acsami.3c02272
ACS Appl. Mater. Interfaces 2023, 15, 26606−26618

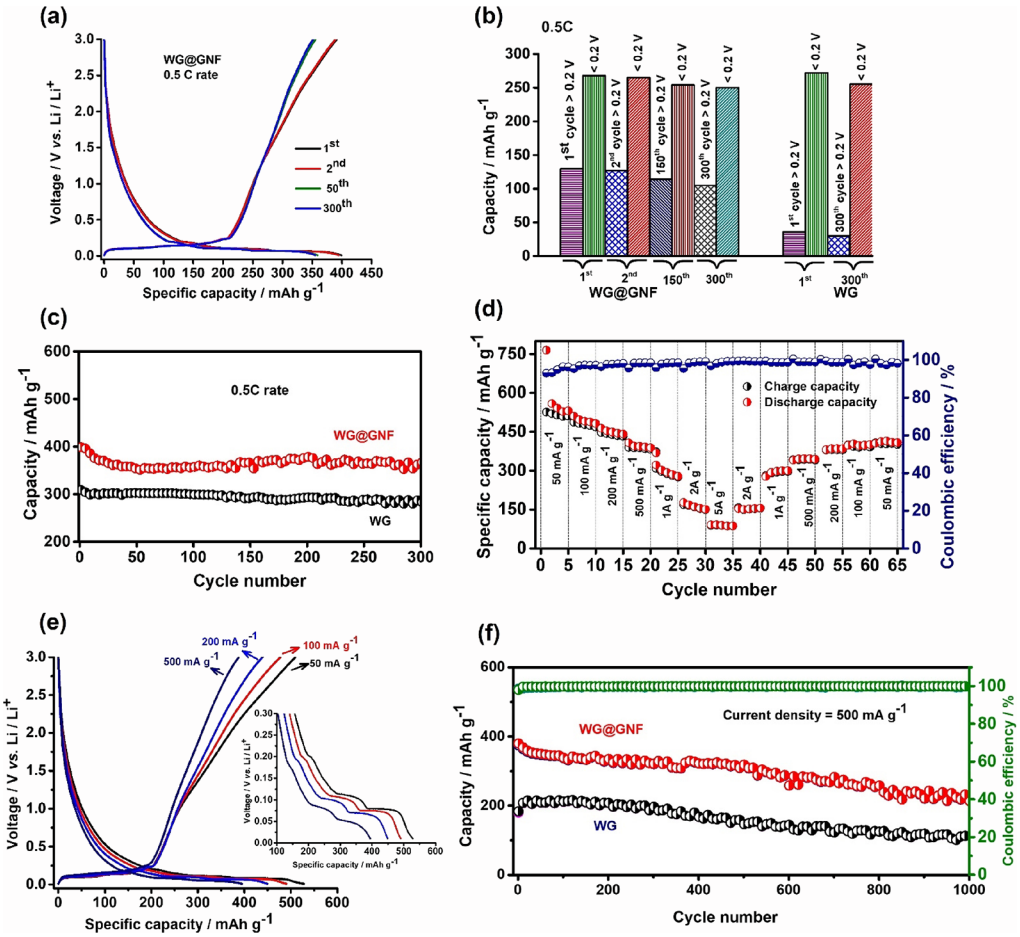

Figure 6. (a) Galvanostatic charge−discharge voltage profile of WG@GNF at 0.5C (1C = 372 mAh g^{-1}) in the voltage range of 0.01−3 V, (b) histogram quantifying the capacity contribution from surface adsorption >0.2 V and intercalation <0.2 V at 0.5C, (c) comparison of cycling stability plot between WG@GNF and WG at 0.5C, (d) C-rate performance, (e) charge−discharge voltage profile of WG@GNF at various current densities (inset: stagewise Li-ion intercalation at lower potential), and (f) comparison of cycling stability plot between WG@GNF and WG at a higher current density of 500 mA g^{-1}.

4, stage 2, and stage 1, respectively, for graphite, whereas the x values are 0.125, 0.25, 0.5, and 0.75 for stage 4′, stage 4″, stage 2', and stage 1, respectively, for the composite. Thus, the resulting specific capacities for stage 4′, stage 4, stage 2, and stage 1 of graphite are 46.5, 93.0, 186.0, and 372.1 mAh g^{-1}, respectively. Similarly, the resulting specific capacities for stage 4′, stage 4″, stage 2', and stage 1 of the composite are 44.1, 88.1, 176.2, and 264.5 mAh g^{-1}, respectively. As can be seen from Figure 5b, the voltage decreases with the increase of Li-ion intercalation for both WG and WG@GNF composite systems during the charging process. The calculated voltages for stage 4′, stage 4, stage 2, and stage 1 are 0.80, 0.35, 0.32, and −0.14 V *vs* Li^+/Li, respectively for WG, whereas the calculated voltages for stage 4′, stage 4″, stage 2', and stage 1 are 2.60, 2.36, 1.27, and 0.74 V *vs* Li^+/Li, respectively, for the WG@GNF composite. Notably, the calculated voltage for stage 1 of graphite shows a negative value, which might be due to the consideration of dispersion correction in DFT to describe the van der Waals interaction accurately.[54] Nevertheless, it is interesting to note that, for a similar range of capacity, the voltage is more in the case of WG@GNF compared to WG. Also, the voltage is higher in the WG@GNF composite than graphite across the studied capacity range, thus matching nicely with the experimental trend. In fact, the voltage of the first intercalation step for each stage is significantly higher than that of the other succeeding intercalation steps, which is in agreement with the experimental result. The reason is expected to be that widening the gap between the layers leads to weakening the van der Waals forces. The enlarged graphite host gallery upon initial Li-intercalation makes subsequent intercalation stages easier. The relative drop of voltage is more in graphite (0.45 V) compared to composite (0.24 V) in the low-capacity region (<50 mAh g^{-1}), reflecting the experimental trend, where the voltage drop has been found to be more in the case of WG compared to WG@GNF. To find out the underlying reason for such drastic voltage drop in graphite, we have analyzed the binding behavior of Li atom into the graphite and composite. To quantify the results, we have calculated the binding energy of a single Li atom into the graphite as well as the composite layer. As shown in the relaxed structure of Figure 5c, the binding energies of Li atom are 0.80 and −3.32 eV into the graphite and composite structure, respectively. The strong binding nature is attributed to the bonding between Li and O atoms, which is reflected in the charge density difference plot also, as shown in the bottom panel of Figure 5c, which clearly shows that the charge accumulation in the graphene layers of graphite structure is more compared to that of the composite structure. Concomitantly, the charge depletion is more at the Li center, thus indicating that the charge depletion in the Li

https://doi.org/10.1021/acsami.3c02272
ACS Appl. Mater. Interfaces 2023, 15, 26606−26618

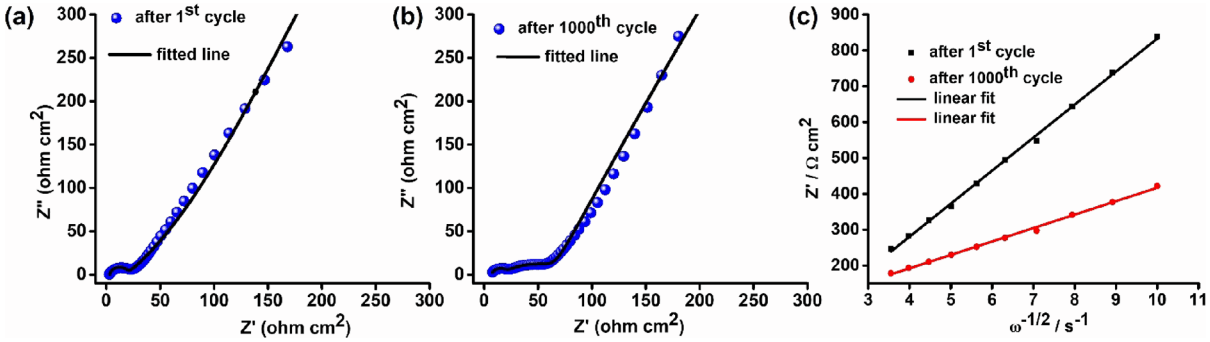

Figure 7. Nyquist plot of the WG@GNF electrode (a) after the 1st cycle and (b) after the 1000th cycle and (c) the corresponding linear fitting between Z' and $\omega^{-1/2}$ in the low-frequency region after the 1st and 1000th cycles.

atom is compensated by the O atom, as evidenced from the accumulated charge density at the O center. Such charge compensation by O atoms retains the trend in case of higher Li concentrations, as shown in Supporting Information Figure S8a. Because the charge transfer is facilitated by O atoms, the follow-up opening of the adjacent gallery becomes thermodynamically more favorable in the case of the composite structure compared to that of the graphite structure. To probe this assumption, we have simulated the Li intercalation in the adjacent layer to the stage 4′ as shown in Supporting Information Figure S8b. The calculated average binding energies of one Li into the adjacent layer are −1.71 and −1.56 eV for composite and graphite systems, respectively. The corresponding CDD plot (bottom panel of Supporting Information Figure S8b) also reveals that charge depletion around the Li atoms is significantly higher in the composite graphite. Therefore, it is established from the binding energy and CDD plot of the second layer intercalation that the lesser charge density at the carbon atoms upon first layer intercalation facilitates the charge transfer between carbon atoms and Li atoms, making the process thermodynamically favorable in the case of the composite, which results in a decrease of the voltage drop in the composite structure compared to the graphite structure.

In this context, we have looked into the electronic behavior of the WG and WG@GNF composite systems to check their nature of electronic conductivity. Supporting Information Figure S9 shows that both WG and WG@GNF systems possess a continuous density of states (DOS) at the Fermi level. However, the composite system shows a more intense DOS at the Fermi level, which can be attributed to the possibility of increased conductivity and a monotonic discharge curve in the composite structure compared to graphite, thus supporting the voltage profile trends.

WG@GNF is exposed to charge−discharge cycling at a higher current density of 0.5C rate after five formation cycles at 0.1C. Figure 6a shows that WG@GNF delivers an enhanced initial stable discharge and charge capacity of 400 and 392 mAh g^{-1}. Figure 6b presents the histogram for the WG@GNF electrode for the 1st, 2nd, 150th, and 300th cycles at 0.5C rate, with a significant contribution of absorption capacity for WG@GNF, which is almost negligible for WG. WG shows relatively lower discharge and charge capacities of 310 and 302 mAh g^{-1} (Figure 6c). At the end of the 300th cycle, WG@GNF and WG exhibit discharge capacities of 354 and 290 mAh g^{-1}, respectively. WG@GNF shows superior cycling stability with an average discharge capacity of 368 mAh g^{-1} with 99% Coulombic efficiency, which is 1.2 times higher than WG at a 0.5C rate, as shown in Figure 6c.

The rate capability studies for WG@GNF and WG are carried out in various current densities (five cycles each) ranging from 50 to 5 A g^{-1}. When the current densities are varied from 50 mA g^{-1} to 100 mA g^{-1}, 200 mA g^{-1}, 500 mA g^{-1}, 1 A g^{-1}, 2 A g^{-1}, and 5 A g^{-1}, WG@GNF shows average specific capacities of 530, 490, 450, 395, 293, 161, and 92 mAh g^{-1}, respectively (Figure 6d). Figure 6e presents the corresponding charge−discharge voltage profile with an inset figure indicating stepwise Li^+ intercalation into the graphite sheets. In comparison, Supporting Information Figure S10 shows that WG delivers negligible capacities at such high current densities. At a current density of 1 A g^{-1}, the capacity enhancement in WG@GNF is 5.8 times compared to WG. On the basis of this observation, we have carried out long-term cycling at 500 mA g^{-1} over 1000 cycles (after 10 formation cycles). Figure 6e shows that WG@GNF exhibits significantly enhanced initial discharge and charge capacities of 380 and 375 mAh g^{-1}. At the 1000th cycle, the capacity becomes 235 mAh g^{-1} with 62% capacity retention with respect to the initial stable capacity. In comparison, WG delivers an average discharge capacity of 156 mAh g^{-1} and 58% capacity retention under similar conditions.

Supporting Information Table S3 presents the present work compared to the reported literature on graphite recycling, indicating the graphite recovery technique, postpurification strategies for enhancing electrochemical activity (including acid washing, catalytic activity, and carbon coating), initial stable discharge capacity, current density, cycle life, and capacity retention.[4,25−31,55,56] It is observed that WG@GNF delivers better capacity value in both a low rate of 0.5C and a high rate of 500 mA g^{-1} with good cycling stability over 1000 charge−discharge cycles, which is superior or at par with the reported literature in terms of cycle number.

Further, to investigate Li^+ kinetics, electrochemical impedance spectroscopy (EIS) is measured for WG@GNF after the 1st cycle (Figure 7a) and the 1000th cycle (Figure 7b), respectively, in the frequency range of 1 MHz to 0.01 Hz. The plots after the first cycle consist of a semicircle in the high-frequency region, indicating charge transfer resistance (R_{CT}), and a linear sloping tail at the low-frequency region, representing Li^+ diffusion into the bulk of the matrix. However, two depressed semicircles appear after cycling. The first semicircle in high frequency is attributed to SEI, and the second one is the charge transfer resistance. R_{CT} values for WG@GNF are increased from 20 Ω cm^2 in the 1st cycle to 67 Ω cm^2 in the 1000th cycle. Li^+ diffusivity is further elucidated

https://doi.org/10.1021/acsami.3c02272
ACS Appl. Mater. Interfaces 2023, 15, 26606−26618

Scheme 2. Pictorial Representation of Different Li^+ Storage Mechanisms of Recycled Graphite, GNF, and WG@GNF

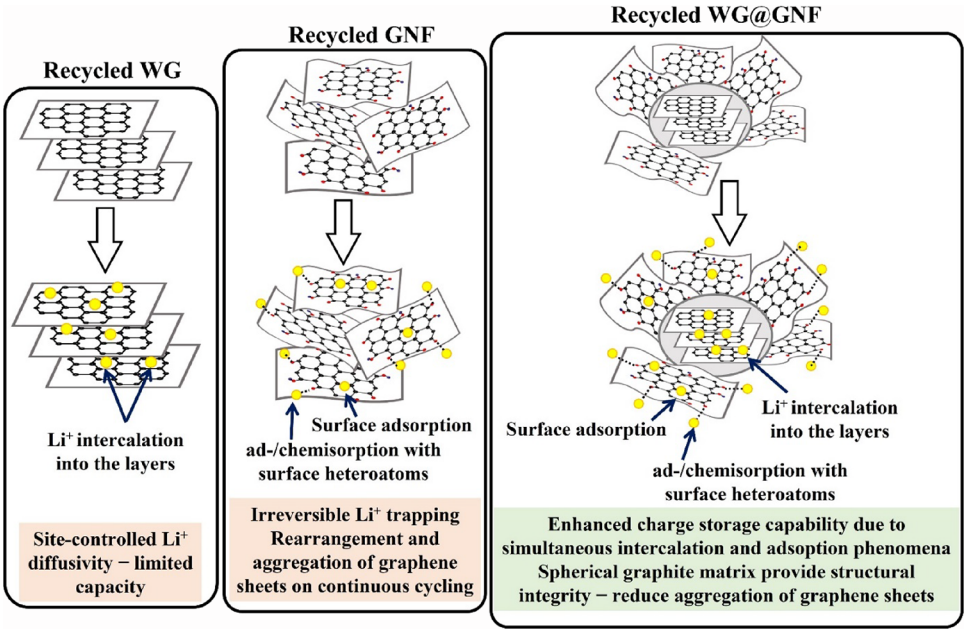

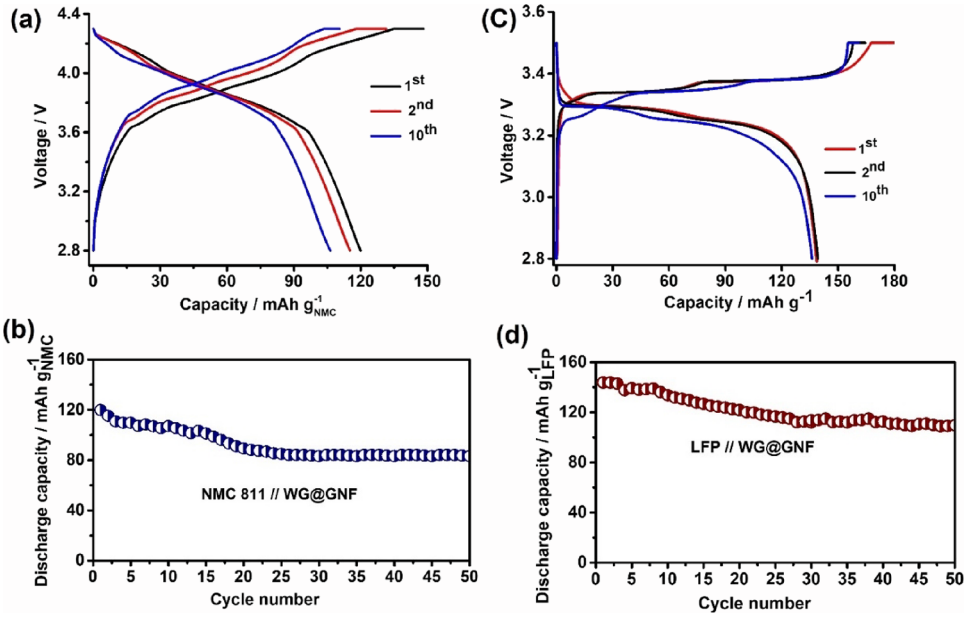

Figure 8. Full cell analysis of (a) charge−discharge voltage profile and (b) discharge capacity *vs* cycle number for the WG@GNF anode and commercial NMC-811 cathode in the voltage window of 2.8−4.3 V, (c) charge−discharge voltage profile, and (d) discharge capacity *vs* cycle number for the WG@GNF anode and commercial LFP cathode in the voltage window of 2.8−3.5 V.

from the EIS spectra at low-frequency regions.[35,36,57] The Warburg factor (σ) of WG@GNF is evaluated from the slope of the plot between Z' and the reciprocal of the square root of frequency ($\omega^{-1/2}$). Figure 7c shows a linear relationship after the 1st and 1000th cycles, and the corresponding slopes (σ) are calculated. It is observed that Li-ion diffusivity at the end of the 1000th cycle (D_{1000}) of the WG@GNF electrode becomes almost 6 times compared to that of the 1st cycle. It might be due to the reorientation of graphene sheets on long-term cycling that generates more space for Li^+ transportation during the lithiation and delithiation process in the WG@GNF electrode. The diffusion coefficient (D) value before and after cycling is compared as follows:

$$D_{1000} = \left[\frac{\sigma_1}{\sigma_{1000}}\right]^2 D_1$$

The above electrochemical studies reveal that the specific capacity of recycled graphite can be enhanced by 1.2−2 times by using recycled graphene as an additive. The voltage profile (Figure 4c) demonstrates that the parabolic sloping voltage curve >2 V incorporates the extra achievable capacities in WG@GNF, which are almost negligible in WG, as observed from the histogram analysis in Figure 4d and Figure 6b. The advanced mechanisms involved in higher charge storage phenomenon, in addition to Li^+ intercalation into the graphite layers, are attributed to (i) more Li-ion accommodation on

https://doi.org/10.1021/acsami.3c02272
ACS Appl. Mater. Interfaces 2023, 15, 26606−26618

both sides and edges of graphene sheets to form LiC_x, (ii) chemiadsorption of Li^+ to the oxygen functionalities as observed from FTIR (Figure 2d) and XPS (Figure 2e) studies, and (iii) nanopore filling of Li^+.[58,59] Moreover, the trapped graphite particles in WG@GNF (as observed from SEM in Figure 1c) might hinder the agglomeration of wrinkled graphene flakes and provides mechanical stability over long-term cycling. Scheme 2 presents the pictorial diagram of different Li^+ storage mechanisms in WG@GNF compared to recycled GNF and WG.

To understand the morphological variations of the WG@GNF anode on continuous cycling, FESEM analysis is carried out after 1000 charge−discharge cycles, as shown in Supporting Information Figure S11. The thickness of the anode coating before the cycling electrode is expanded from 20−25 (Supporting Information Figure S11a) to 50−55 μm (Supporting Information Figure S11b) for the after-cycled electrode. Supporting Information Figure S11c,d indicates the appearance of SEI surface film-like secondary particles and deposition of new particles, which are expected to comprise of inorganic Li salts (e.g., Li_2O, Li_2CO_3, Li alkyl carbonates, and LiF) and organic oligomers (ROCOOLi and ROLi, where R is alkyl groups of low molecular weight) that are formed via reductive decomposition of the electrolyte. Further, to check the practical feasibility of the WG@GNF anode, full cells are fabricated with commercial NMC 811 and LFP cathode. The cathode and anode weight ratio is maintained at ∼2.8:1. The capacity *vs* voltage profile for NMC 811 and LFP cathode at 0.1C rate shows that the half-cells deliver an average capacity of 180 and 160 mAh g^{-1}, respectively, as shown in Supporting Information Figure S12a,b. The full cells fabricated with NMC811//WG@GNF and LFP//WG@GNF deliver an initial discharge capacity of 120 and 140 mAh g^{-1} at C/3 rate in the voltage window of 2.8−4.3 and 2.8−3.5 V, respectively, and the cells show quite stable electrochemical performance (Figure 8). This study manifests that the electrochemical activity of spent graphite anode can be revitalized, and recycled WG@GNF is a promising anode material for high-performance LIBs.

CONCLUSIONS

The recovery of value-added electrode materials from spent LIBs such as Li, transition metals (Co, Ni, Mn), and battery-grade graphite has been studied in recent years for economic incentives and resource sustainability. The advantage of the retention of the bulk structural integrity of the cycled graphite has garnered much interest for second-life Li-ion storage. Herein, the anode graphite material is recovered from spent LIBs by water leaching followed by postpurification via inert-atmosphere calcination to enhance the degree of graphitization. Graphene nanoflakes (GNFs) are prepared from the recovered water-washed graphite (WG) by Hummer's method followed by thermal reduction. Electrochemistry depicts that the pure GNF anode experiences a very high irreversible capacity loss (∼50%) during initial cycles due to irreversible Li^+ trapping in surface heteroatom functionalities, defect sites, and nanopore filling. Despite being a high-capacity anode material, this causes a big hurdle for commercializing pure graphene systems. However, the high charge-storage capability of GNF can be utilized, and the site-limited diffusivity of recycled graphite anode can be enhanced by amalgamating an optimized amount of GNF additive (i.e., 20 wt %) to the recycled WG matrix with a proper balancing between high specific capacity and long-term cycling stability. The extra achievable capacity in WG@GNF originates from more Li-ion intercalation into larger d-spacing (as observed in the XRD plot) and chemisorption to the controlled surface functionalities (as observed in FTIR, XPS, and EDX analysis). A synergistic phenomenon composed of Li-ion adsorption (sloping region capacity) and intercalation (plateau region capacity) in WG@GNF resulted in enhanced average capacities of ∼368 mAh g^{-1} at 0.5C over 300 cycles and ∼320 mAh g^{-1} at a higher current density of 500 mA g^{-1} over 1000 cycles, which are almost 1.2−2 times in comparison to those of recovered WG (∼295 mAh g^{-1} at 0.5C and ∼156 mAh g^{-1} at 500 mA g^{-1}). The electrochemistry results are further supported by DFT calculations considering the WG@GNF and WG models. The DFT results demonstrate that the strong Li adsorption with oxygen functionalized sites plays a key role in the low voltage drop across the sloping capacity region. Additionally, it has been established that the thermodynamic feasibility of the Li-ion intercalation process is attributed to the charge density of the layers of the graphite. Besides, the unique SEM morphology of entrapping spherical graphite particles among wrinkled graphene flakes reduces their crumbling and provides structural stability over long-term cycling. Impedance studies display that the WG@GNF anode facilitates almost 6 times more diffusivity at the end of the 1000th cycle. To showcase the practical feasibility of the WG@GNF anode, the full cell is fabricated with the commercial LFP and NMC-811 cathode that demonstrates optimum electrochemical performance. It is believed that WG@GNF is a potentially feasible anode material for upscaling applications. This strategy paves a sustainable and economically viable avenue to improvise the electrochemical compatibility of recycled graphite anode from spent Li-ion batteries.

ASSOCIATED CONTENT

Supporting Information

The Supporting Information is available free of charge at https://pubs.acs.org/doi/10.1021/acsami.3c02272.

Reported graphene-carbon composite and electrochemistry in comparison to our studies; computational models for WG and WG@GNF; EDS of recovered graphite, purified graphite, and WG@GNF; TEM images of WG and GNF; XRD of GNF; simulated XRD; optimization of GNF additive in capacity *vs* voltage profile and the comparative study of irreversible capacity; CV of GNF; CDD plot; density of states; C-rate for WG; FESEM image before and after cycling WG@GNF electrode; a comparison table between the reported literature and the present study indicating anode recovery, postpurification strategy, and their electrochemical performance; and capacity *vs* voltage profile for NMC 811 and LFP cathode (PDF)

AUTHOR INFORMATION

Corresponding Authors

Arup Mahata − *Department of Chemistry, Indian Institute of Technology Hyderabad, Sangareddy 502284 Telangana, India;* orcid.org/0000-0002-4995-3326; Email: arup@chy.iith.ac.in

Surendra K. Martha − *Department of Chemistry, Indian Institute of Technology Hyderabad, Sangareddy 502284*

https://doi.org/10.1021/acsami.3c02272
ACS Appl. Mater. Interfaces 2023, 15, 26606−26618

Telangana, India; orcid.org/0000-0002-7762-7237; Email: martha@chy.iith.ac.in

Authors

Madhushri Bhar − *Department of Chemistry, Indian Institute of Technology Hyderabad, Sangareddy 502284 Telangana, India*

Udita Bhattacharjee − *Department of Chemistry, Indian Institute of Technology Hyderabad, Sangareddy 502284 Telangana, India*

Dhritismita Sarma − *Department of Chemistry, Indian Institute of Technology Hyderabad, Sangareddy 502284 Telangana, India*

Satheesh Krishnamurthy − *School of Engineering & Innovation, The Open University, Milton Keynes MK7 6AA, U.K.;* orcid.org/0000-0001-7237-9206

Kaliprasad Yalamanchili − *Nile Limited, Hyderabad 500034 Telangana, India*

Complete contact information is available at: https://pubs.acs.org/10.1021/acsami.3c02272

Author Contributions

Madhushri Bhar: conceptualization, methodology, experimental analysis, data curation, writing−review & editing. Udita Bhattacharjee: formal analysis, data curation. Dhritismita Sarma: investigation, formal analysis of theoretical studies. Satheesh Krishnamurthy: project administration, funding acquisition. Kaliprasad Yalamanchili: resources, validation, industry coordinator. Arup Mahata: formal analysis of theoretical studies, writing computational aspects of the manuscript and editing. Surendra K. Martha: methodology, supervision, conceptualization, writing−review & editing, funding acquisition.

Notes

The authors declare no competing financial interest.

■ ACKNOWLEDGMENTS

M.B. and U.B. acknowledge DST-INSPIRE (code: IF180708), the Ministry of Science and Technology, and the Ministry of Education, Govt. of India, for the fellowship. S.K.M. acknowledges the UKIERI program under grant DST/INT/UK/P-173/2017, Govt. of India, for the funding. S.K.M. and S.K. further acknowledge partial funds from the Royal Academy of Engineering (Academic reference IAPP1R2\100125) for the initial support of this work. D.S. acknowledges the Ministry of Education, Govt. of India, for the fellowship.

■ REFERENCES

(1) Li, M.; Lu, J.; Chen, Z.; Amine, K. 30 Years of Lithium-Ion Batteries. *Adv. Mater.* **2018**, *30*, 1800561.

(2) Manthiram, A. An Outlook on Lithium Ion Battery Technology. *ACS Cent. Sci.* **2017**, *3*, 1063−1069.

(3) Wang, Y.; An, N.; Wen, L.; Wang, L.; Jiang, X.; Hou, F.; Yin, Y.; Liang, J. Recent Progress on the Recycling Technology of Li-Ion Batteries. *J. Energy Chem.* **2021**, *55*, 391−419.

(4) Ma, X.; Chen, M.; Chen, B.; Meng, Z.; Wang, Y. High-Performance Graphite Recovered from Spent Lithium-Ion Batteries. *ACS Sustainable Chem. Eng.* **2019**, *7*, 19732−19738.

(5) Gu, K.; Chang, J.; Mao, X.; Zeng, H.; Qin, W.; Han, J. Efficient Separation of Cathode Materials and Al Foils from Spent Lithium Batteries with Glycerol Heating: A Green and Unconventional Way. *J. Cleaner Prod.* **2022**, *369*, No. 133270.

(6) Moradi, B.; Botte, G. G. Recycling of Graphite Anodes for the next Generation of Lithium Ion Batteries. *J. Appl. Electrochem.* **2016**, *46*, 123−148.

(7) Zhang, J.; Lei, Y.; Lin, Z.; Xie, P.; Lu, H.; Xu, J. A Novel Approach to Recovery of Lithium Element and Production of Holey Graphene Based on the Lithiated Graphite of Spent Lithium Ion Batteries. *Chem. Eng. J.* **2022**, *436*, No. 135011.

(8) Yeware, K. Graphite Market by Type (Natural Graphite and Synthetic Graphite) and Application (Lubrication, Refractories, Foundry, Battery Production, and Others): Global Opportunity Analysis and Industry Forecast, 2019−2027. *Bulk Chem.* **2020**, A01635.

(9) Yang, L.; Gao, Z.; Liu, T.; Huang, M.; Liu, G.; Feng, Y.; Shao, P.; Luo, X. Direct Electrochemical Leaching Method for High-Purity Lithium Recovery from Spent Lithium Batteries. *Environ. Sci. Technol.* **2023**, *57*, 4591−4597.

(10) Yang, L.; Feng, Y.; Wang, C.; Fang, D.; Yi, G.; Gao, Z.; Shao, P.; Liu, C.; Luo, X.; Luo, S. Closed-Loop Regeneration of Battery-Grade FePO4 from Lithium Extraction Slag of Spent Li-Ion Batteries via Phosphoric Acid Mixture Selective Leaching. *Chem. Eng. J.* **2022**, *431*, No. 133232.

(11) Zhou, M.; Li, B.; Li, J.; Xu, Z. Pyrometallurgical Technology in the Recycling of a Spent Lithium Ion Battery: Evolution and the Challenge. *ACS EST Engg.* **2021**, *1*, 1369−1382.

(12) Rey, I.; Vallejo, C.; Santiago, G.; Iturrondobeitia, M.; Lizundia, E. Environmental Impacts of Graphite Recycling from Spent Lithium-Ion Batteries Based on Life Cycle Assessment. *ACS Sustainable Chem. Eng.* **2021**, *9*, 14488−14501.

(13) Park, C.-M.; Kim, J.-H.; Kim, H.; Sohn, H.-J. Li-Alloy Based Anode Materials for Li Secondary Batteries. *Chem. Soc. Rev.* **2010**, *39*, 3115−3141.

(14) Elias, L.; Bhar, M.; Ghosh, S.; Martha, S. K. Effect of Alloying on the Electrochemical Performance of Sb and Sn Deposits as an Anode Material for Lithium-Ion and Sodium-Ion Batteries. *Ionics* **2022**, *28*, 2759−2768.

(15) Abouimrane, A.; Compton, O. C.; Amine, K.; Nguyen, S. T. Non-Annealed Graphene Paper as a Binder-Free Anode for Lithium-Ion Batteries. *J. Phys. Chem. C* **2010**, *114*, 12800−12804.

(16) Yoo, E.; Kim, J.; Hosono, E.; Zhou, H.; Kudo, T.; Honma, I. Large Reversible Li Storage of Graphene Nanosheet Families for Use in Rechargeable Lithium Ion Batteries. *Nano Lett.* **2008**, *8*, 2277−2282.

(17) Liu, Y.; Artyukhov, V. I.; Liu, M.; Harutyunyan, A. R.; Yakobson, B. I. Feasibility of Lithium Storage on Graphene and Its Derivatives. *J. Phys. Chem. Lett.* **2013**, *4*, 1737−1742.

(18) Dufficy, M. K.; Khan, S. A.; Fedkiw, P. S. Hierarchical Graphene-Containing Carbon Nanofibers for Lithium-Ion Battery Anodes. *ACS Appl. Mater. Interfaces* **2016**, *8*, 1327−1336.

(19) Zhang, J.; Cao, H.; Tang, X.; Fan, W.; Peng, G.; Qu, M. Graphite/Graphene Oxide Composite as High Capacity and Binder-Free Anode Material for Lithium Ion Batteries. *J. Power Sources* **2013**, *241*, 619−626.

(20) Agostini, M.; Brutti, S.; Hassoun, J. High Voltage Li-Ion Battery Using Exfoliated Graphite/Graphene Nanosheets Anode. *ACS Appl. Mater. Interfaces* **2016**, *8*, 10850−10857.

(21) Zhang, J.; Xie, Z.; Li, W.; Dong, S.; Qu, M. High-Capacity Graphene Oxide/Graphite/Carbon Nanotube Composites for Use in Li-Ion Battery Anodes. *Carbon* **2014**, *74*, 153−162.

(22) Lee, S.-H.; Seo, S.-D.; Jin, Y.-H.; Shim, H.-W.; Kim, D.-W. A Graphite Foil Electrode Covered with Electrochemically Exfoliated Graphene Nanosheets. *Electrochem. Commun.* **2010**, *12*, 1419−1422.

(23) Aurbach, D.; Zinigrad, E.; Cohen, Y.; Teller, H. A Short Review of Failure Mechanisms of Lithium Metal and Lithiated Graphite Anodes in Liquid Electrolyte Solutions. *Solid State Ionics* **2002**, *148*, 405−416.

(24) Peled, E.; Menkin, S. Review—SEI: Past, Present and Future. *J. Electrochem. Soc.* **2017**, *164*, A1703−A1719.

(25) Yang, Y.; Song, S.; Lei, S.; Sun, W.; Hou, H.; Jiang, F.; Ji, X.; Zhao, W.; Hu, Y. A Process for Combination of Recycling Lithium

and Regenerating Graphite from Spent Lithium-Ion Battery. *Waste Manage.* **2019**, *85*, 529−537.
(26) Liu, K.; Yang, S.; Luo, L.; Pan, Q.; Zhang, P.; Huang, Y.; Zheng, F.; Wang, H.; Li, Q. From Spent Graphite to Recycle Graphite Anode for High-Performance Lithium Ion Batteries and Sodium Ion Batteries. *Electrochim. Acta* **2020**, *356*, No. 136856.
(27) Zhang, J.; Li, X.; Song, D.; Miao, Y.; Song, J.; Zhang, L. Effective Regeneration of Anode Material Recycled from Scrapped Li-Ion Batteries. *J. Power Sources* **2018**, *390*, 38−44.
(28) Chen, Q.; Huang, L.; Liu, J.; Luo, Y.; Chen, Y. A New Approach to Regenerate High-Performance Graphite from Spent Lithium-Ion Batteries. *Carbon* **2022**, *189*, 293−304.
(29) Xiao, H.; Ji, G.; Ye, L.; Li, Y.; Zhang, J.; Ming, L.; Zhang, B.; Ou, X. Efficient Regeneration and Reutilization of Degraded Graphite as Advanced Anode for Lithium-Ion Batteries. *J. Alloys Compd.* **2021**, *888*, No. 161593.
(30) Xiao, Y.; Li, J.; Huang, W.; Wang, L.; Luo, J. Green & Efficient Regeneration of Graphite Anode from Spent Lithium Ion Batteries Enabled by Asphalt Coating. *J. Mater. Sci.: Mater. Electron.* **2022**, *33*, 16740−16752.
(31) Ma, Z.; Zhuang, Y.; Deng, Y.; Song, X.; Zuo, X.; Xiao, X.; Nan, J. From Spent Graphite to Amorphous Sp2+ Sp3 Carbon-Coated Sp2 Graphite for High-Performance Lithium Ion Batteries. *J. Power Sources* **2018**, *376*, 91−99.
(32) Gao, Y.; Wang, C.; Zhang, J.; Jing, Q.; Ma, B.; Chen, Y.; Zhang, W. Graphite Recycling from the Spent Lithium-Ion Batteries by Sulfuric Acid Curing−Leaching Combined with High-Temperature Calcination. *ACS Sustainable Chem. Eng.* **2020**, *8*, 9447−9455.
(33) Zhu, A.; Bian, X.; Han, W.; Wen, Y.; Ye, K.; Wang, G.; Yan, J.; Cao, D.; Zhu, K.; Wang, S. Microwave-Ultra-Fast Recovery of Valuable Metals from Spent Lithium-Ion Batteries by Deep Eutectic Solvents. *Waste Manage.* **2023**, *156*, 139−147.
(34) Zhu, A.; Bian, X.; Han, W.; Cao, D.; Wen, Y.; Zhu, K.; Wang, S. The Application of Deep Eutectic Solvents in Lithium-Ion Battery Recycling: A Comprehensive Review. *Resour., Conserv. Recycl.* **2023**, *188*, No. 106690.
(35) Bhar, M.; Dey, A.; Ghosh, S.; van Spronsen, M. A.; Selvaraj, V.; Kaliprasad, Y.; Krishnamurthy, S.; Martha, S. K. Plasma Jet Printing Induced High-Capacity Graphite Anodes for Sustainable Recycling of Lithium-Ion Batteries. *Carbon* **2022**, *198*, 401−410.
(36) Bhar, M.; Ghosh, S.; Krishnamurthy, S.; Yalamanchili, K.; Martha, S. K. Electrochemical Compatibility of Graphite Anode from Spent Li-Ion Batteries: Recycled via a Greener and Sustainable Approach. *ACS Sustainable Chem. Eng.* **2022**, *10*, 7515−7525.
(37) Wang, H.; Huang, Y.; Huang, C.; Wang, X.; Wang, K.; Chen, H.; Liu, S.; Wu, Y.; Xu, K.; Li, W. Reclaiming Graphite from Spent Lithium Ion Batteries Ecologically and Economically. *Electrochim. Acta* **2019**, *313*, 423−431.
(38) Naresh, V.; Bhattacharjee, U.; Martha, S. K. Boron Doped Graphene Nanosheets as Negative Electrode Additive for High-Performance Lead-Acid Batteries and Ultracapacitors. *J. Alloys Compd.* **2019**, *797*, 595−605.
(39) Scandolo, S.; Giannozzi, P.; Cavazzoni, C.; de Gironcoli, S.; Pasquarello, A.; Baroni, S. First-Principles Codes for Computational Crystallography in the Quantum-ESPRESSO Package. *Z. Kristallogr. Cryst. Mater.* **2005**, *220*, 574−579.
(40) Giannozzi, P.; Andreussi, O.; Brumme, T.; Bunau, O.; Buongiorno Nardelli, M.; Calandra, M.; Car, R.; Cavazzoni, C.; Ceresoli, D.; Cococcioni, M.; Colonna, N.; Carnimeo, I.; Dal Corso, A.; de Gironcoli, S.; Delugas, P.; DiStasio, R. A., Jr.; Ferretti, A.; Floris, A.; Fratesi, G.; Fugallo, G.; Gebauer, R.; Gerstmann, U.; Giustino, F.; Gorni, T.; Jia, J.; Kawamura, M.; Ko, H.-Y.; Kokalj, A.; Küçükbenli, E.; Lazzeri, M.; Marsili, M.; Marzari, N.; Mauri, F.; Nguyen, N. L.; Nguyen, H.-V.; Otero-de-la-Roza, A.; Paulatto, L.; Poncé, S.; Rocca, D.; Sabatini, R.; Santra, B.; Schlipf, M.; Seitsonen, A. P.; Smogunov, A.; Timrov, I.; Thonhauser, T.; Umari, P.; Vast, N.; Wu, X.; Baroni, S. Advanced Capabilities for Materials Modelling with Quantum ESPRESSO. *J. Phys.: Condens. Matter* **2017**, *29*, 465901.
(41) Grimme, S.; Antony, J.; Ehrlich, S.; Krieg, H. A Consistent and Accurate Ab Initio Parametrization of Density Functional Dispersion Correction (DFT-D) for the 94 Elements H-Pu. *J. Chem. Phys.* **2010**, *132*, 154104.
(42) Monkhorst, H. J.; Pack, J. D. Special Points for Brillouin-Zone Integrations. *Phys. Rev. B* **1976**, *13*, 5188−5192.
(43) Aydinol, M. K.; Kohan, A. F.; Ceder, G.; Cho, K.; Joannopoulos, J. *Ab Initio* Study of Lithium Intercalation in Metal Oxides and Metal Dichalcogenides. *Phys. Rev. B* **1997**, *56*, 1354−1365.
(44) Bhauriyal, P.; Mahata, A.; Pathak, B. The Staging Mechanism of $AlCl_4$ Intercalation in a Graphite Electrode for an Aluminium-Ion Battery. *Phys. Chem. Chem. Phys.* **2017**, *19*, 7980−7989.
(45) Bhauriyal, P.; Mahata, A.; Pathak, B. Graphene-like Carbon−Nitride Monolayer: A Potential Anode Material for Na- and K-Ion Batteries. *J. Phys. Chem. C* **2018**, *122*, 2481−2489.
(46) Aydinol, M. K.; Kohan, A. F.; Ceder, G. Ab Initio Calculation of the Intercalation Voltage of Lithium-Transition-Metal Oxide Electrodes for Rechargeable Batteries. *J. Power Sources* **1997**, *68*, 664−668.
(47) Er, D.; Li, J.; Naguib, M.; Gogotsi, Y.; Shenoy, V. B. Ti_3C_2 MXene as a High Capacity Electrode Material for Metal (Li, Na, K, Ca) Ion Batteries. *ACS Appl. Mater. Interfaces* **2014**, *6*, 11173−11179.
(48) Ashton, M.; Hennig, R. G.; Sinnott, S. B. Computational Characterization of Lightweight Multilayer MXene Li-Ion Battery Anodes. *Appl. Phys. Lett.* **2016**, *108*, No. 023901.
(49) Kumar, S.; Choudhuri, I.; Pathak, B. An Atomically Thin Ferromagnetic Half-Metallic Pyrazine-Fused Mn-Porphyrin Sheet: A Slow Spin Relaxation System. *J. Mater. Chem. C* **2016**, *4*, 9069−9077.
(50) Garg, P.; Kumar, S.; Choudhuri, I.; Mahata, A.; Pathak, B. Hexagonal Planar CdS Monolayer Sheet for Visible Light Photocatalysis. *J. Phys. Chem. C* **2016**, *120*, 7052−7060.
(51) Fang, Y.; Lv, Y.; Che, R.; Wu, H.; Zhang, X.; Gu, D.; Zheng, G.; Zhao, D. Two-Dimensional Mesoporous Carbon Nanosheets and Their Derived Graphene Nanosheets: Synthesis and Efficient Lithium Ion Storage. *J. Am. Chem. Soc.* **2013**, *135*, 1524−1530.
(52) Kumar, S.; Bhauriyal, P.; Pathak, B. Computational Insights into the Working Mechanism of the LiPF6−Graphite Dual-Ion Battery. *J. Phys. Chem. C* **2019**, *123*, 23863−23871.
(53) Van der Ven, A.; Deng, Z.; Banerjee, S.; Ong, S. P. Rechargeable Alkali-Ion Battery Materials: Theory and Computation. *Chem. Rev.* **2020**, *120*, 6977−7019.
(54) Persson, K.; Hinuma, Y.; Meng, Y. S.; Van der Ven, A.; Ceder, G. Thermodynamic and Kinetic Properties of the Li-Graphite System from First-Principles Calculations. *Phys. Rev. B* **2010**, *82*, No. 125416.
(55) Dong, S.; Song, Y.; Ye, K.; Yan, J.; Wang, G.; Zhu, K.; Cao, D. Ultra-Fast, Low-Cost, and Green Regeneration of Graphite Anode Using Flash Joule Heating Method. *EcoMat* **2022**, *4*, No. e12212.
(56) Liu, J.; Shi, H.; Yu, K.; Geng, Y.; Hu, X.; Yi, G.; Zhang, J.; Luo, X. Regeneration and Reuse of Anode Graphite from Spent Lithium-Ion Batteries with Low Greenhouse Gas (GHG) Emissions. *Chin. Chem. Lett.* **2023**, *108274*, No. 108274.
(57) Narsimulu, D.; Ghosh, S.; Bhar, M.; Martha, S. K. Electrochemical Studies on Kinetics and Diffusion of Li-Ions in MnO_2 Electrodes. *J. Electrochem. Soc.* **2019**, *166*, A2629−A2635.
(58) Bhattacharjee, U.; Bhowmik, S.; Ghosh, S.; Vangapally, N.; Martha, S. K. Boron-Doped Graphene Anode Coupled with Microporous Activated Carbon Cathode for Lithium-Ion Ultracapacitors. *Chem. Eng. J.* **2022**, *430*, No. 132835.
(59) Mukherjee, R.; Thomas, A. V.; Datta, D.; Singh, E.; Li, J.; Eksik, O.; Shenoy, V. B.; Koratkar, N. Defect-Induced Plating of Lithium Metal within Porous Graphene Networks. *Nat. Commun.* **2014**, *5*, 3710.

https://doi.org/10.1021/acsami.3c02272
ACS Appl. Mater. Interfaces 2023, 15, 26606−26618